THE ASTROPHYSICAL JOURNAL SUPPLEMENT SERIES, 120:399–408, 1999 February
© 1999. The American Astronomical Society. All rights reserved. Printed in U.S.A.

THE *ULYSSES* SUPPLEMENT TO THE BATSE 3B CATALOG OF COSMIC GAMMA-RAY BURSTS

K. HURLEY
University of California, Berkeley, Space Sciences Laboratory, Berkeley, CA 94720-7450; khurley@sunspot.ssl.berkeley.edu
M. S. BRIGGS AND R. M. KIPPEN
University of Alabama, Huntsville, Huntsville, AL 35899
C. KOUVELIOTOU,[1] C. MEEGAN, AND G. FISHMAN
NASA Marshall Space Flight Center, Huntsville, AL 35812
T. CLINE
NASA Goddard Space Flight Center, Code 661, Greenbelt, MD 20771
AND
M. BOER
Centre d'Etude Spatiale des Rayonnements, B.P. 4346, 31029 Toulouse, France
Received 1998 March 12; accepted 1998 October 21

ABSTRACT

We present interplanetary network localization information for 218 gamma-ray bursts in the third BATSE catalog obtained by analyzing the arrival times of these bursts with the *Ulysses* and *Compton Gamma Ray Observatory* spacecraft. For any given burst observed by these two spacecraft, arrival time analysis (or "triangulation") results in an annulus of possible arrival directions whose half-width varies between 7″ and 32′, depending on the intensity and time history of the burst and the distance of the *Ulysses* spacecraft from Earth. This annulus generally intersects the BATSE error circle, which results in an average reduction of a factor of 30 of the error box area.

Subject headings: catalogs — gamma rays: bursts

1. INTRODUCTION

A knowledge of the precise positions of cosmic gamma-ray bursts (GRBs) is important for many studies. For example, recent observations of the optical counterparts to bursts have provided evidence that at least two of them are at cosmological distances (Metzger et al. 1997; Kulkarni et al. 1998), and therefore, by implication, most or all of them may also be at such distances. One optical counterpart has been associated with a galaxy, and the majority of the models for the energy release in bursts have long invoked neutron star–neutron star or neutron star–black hole mergers (see, e.g., Paczyński 1991). If this is correct, GRBs should originate in or close to galaxies, and correlations between burst positions and the large-scale structure of the universe might be expected. In this context, it has been debated whether the positions of bursts are correlated with those of Abell clusters (Kolatt & Piran 1996; Hurley et al. 1997a; Struble & Rood 1997) and radio-quiet quasars (Hurley et al. 1997b; Schartel, Andernach, & Greiner 1997). In both cases, increased precision in the location accuracy leads to more stringent tests. Similarly, precise positions greatly improve searches for quiescent counterparts to GRBs in other wavelength ranges (see, e.g., Tokanai et al. 1997) and can help confirm proposed associations between GRBs and fading counterparts (Hurley et al. 1997c). Finally, burst recurrence from a single source is excluded in most cosmological models. Such recurrence would reveal itself through small-scale clustering in the angular distribution of burst locations, and the sensitivity of the distribution function to repeating sources is greater when the burst location accuracy is improved (Kippen, Hurley, & Pendleton 1998).

We present here a catalog from the detector aboard the *Ulysses* spacecraft of 218 GRBs that were also observed by the Burst and Transient Source Experiment (BATSE) and cataloged in the BATSE 3B catalog (Meegan et al. 1996). In the present catalog, their positions have been improved in accuracy by arrival time analysis, or "triangulation." Detection of an event by these two widely separated instruments leads to a narrow annulus that intersects the BATSE error circle and reduces its area by a factor of ≈ 30. Such annulus/error circle intersections have played important roles in the examples cited above.

2. INSTRUMENTATION

The *Ulysses* GRB detector (Hurley et al. 1992) is one instrument in the third interplanetary network of burst detectors. It consists of two 3 mm thick hemispherical CsI scintillators with a projected area of about 20 cm^2 in any direction. The detector is mounted on a magnetometer boom far from the body of the spacecraft, and therefore has a practically unobstructed view of the full sky. Because the *Ulysses* mission is in interplanetary space, the instrument also benefits from an exceptionally stable background. The GRB detector operates continuously, and over 97% of the data are recovered.

A unique feature of the mission is the fact that it is in heliocentric orbit with aphelion ≈ 5 AU. Thus it reaches an apogee of ≈ 6 AU or 3000 lt-s, and during portions of the orbit the GRB experiment is farther than any burst detector has ever been from Earth, which results in greatly improved location accuracies for GRBs.

The GRB instrument observes bursts in both a triggered and a real-time mode. The triggered mode is initiated when the number of counts in one of two possible time intervals exceeds a preset value. Because the background is stable, this number is defined in terms of an absolute number of

[1] Universities Space Research Association, Marshall Space Flight Center ES-84, Huntsville, AL 35812.

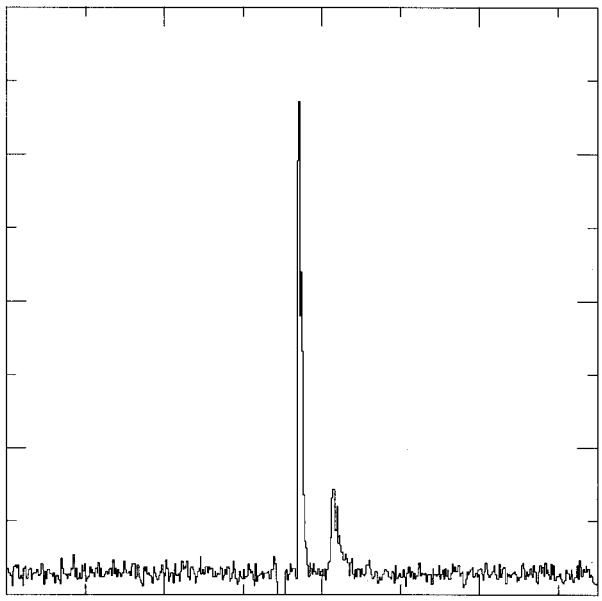

FIG. 1.—*Ulysses* triggered data. The response to BATSE burst 2151 on 1993 January 31 is shown. The time resolution is 0.03125 s.

counts, rather than a number of standard deviations above the background. The two time intervals may be selected among values from 0.125 to 4 s. Each of the two time intervals is associated with an independently selectable energy window whose lower and upper thresholds lie between ≈ 15 and 150 keV. The data collected in the triggered mode consist of energy spectra, and either 16 s of 8 ms count rates, or 64 s of 32 ms count rates, in the $\approx$25–150 keV energy range; ≈ 1.8 and 7.4 s of the data stream record the time histories prior to trigger, respectively. Following a trigger, data are read out for ≈ 40 m, during which time the experiment cannot retrigger. An example is shown in Figure 1.

Independent of the trigger, a continuous stream of real-time data is transmitted. This consists of count rates taken with 0.25, 0.5, 1, or 2 s time resolution. The resolution depends on the spacecraft telemetry rate, and the energy range is $\approx$25–150 keV, as it is for the trigger. Data are compressed in this mode. An example is shown in Figure 2. The real-time data serve many purposes. For example, numerous GRBs that are not intense enough to trigger the detector can be reliably identified in the real-time data, as we demonstrate below. Bursts arriving during trigger readout may also be identified. Finally, bursts whose duration exceeds the duration of the triggered memory can be fully recorded in this mode.

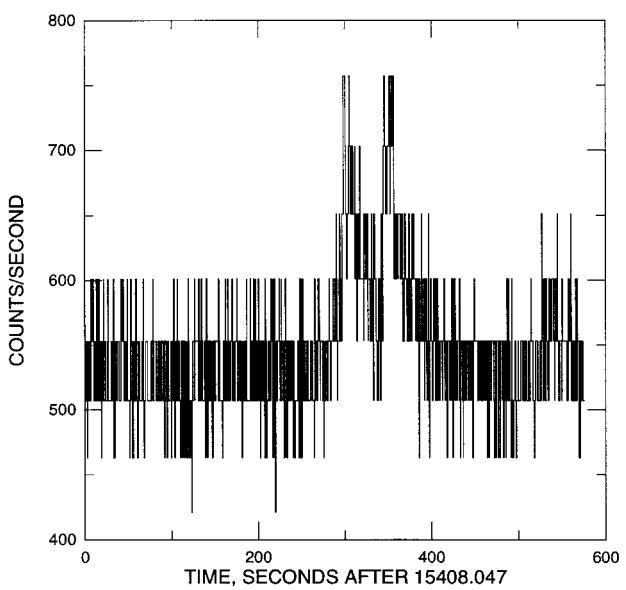

FIG. 2.—*Ulysses* GRB 0.5 s resolution real-time data for the crossing window for BATSE burst 1008 on 1991 November 6. BATSE observed only the first peak of this event before entering the South Atlantic Anomaly. *Ulysses* GRB triggered on the second peak. The "quantized" appearance of the data is due to compression.

BATSE consists of eight detector modules situated at the corners of the *Compton Gamma Ray Observatory* (*CGRO*) spacecraft. Each contains a large area detector (LAD), a 50.8 cm diameter by 1.27 cm thick NaI scintillator. The trigger algorithm examines the count rates of two or more detectors in the 50–300 keV energy range, over 64, 256, and 1024 ms intervals. The experiment is described in more detail in Meegan et al. (1996). For most of the events in this catalog, we have utilized the DISCSC and PREB data types summed over two, three, or four detectors. This gives a 0.064 s resolution time history from 2 s prior to the trigger to 240 s or more after the trigger. We selected discriminator channels 1 and 2 corresponding to the energy range 25–100 keV to match the *Ulysses* energy range as closely as possible. Rarely, this data type is not available; in that case we use MER, TTS, TTE, or 1 s resolution data. As BATSE is in low Earth orbit, the time history data are occasionally interrupted by data gaps and Earth occultation.

3. SEARCH PROCEDURE

Every cosmic burst detected by BATSE is systematically searched for in the *Ulysses* data as soon as the BATSE data are available for it. This is done by using the approximate arrival direction from BATSE and the position of the *Ulysses* spacecraft to calculate a range of possible arrival times at *Ulysses*. The calculation assumes generous uncertainties in the arrival direction to assure that the crossing window always includes the burst. Typical window lengths are 300–500 s (e.g., Fig. 2). In cases where the BATSE positions undergo substantial revision, a revised search window is calculated and the search is redone.

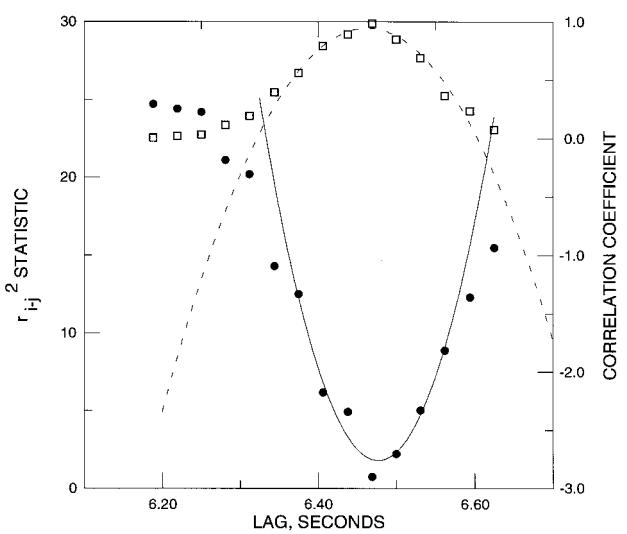

FIG. 3.—r^2_{ij} (*circles*) and correlation coefficient ρ_{ij} (*squares*) as a function of lag for the burst of Fig. 1, and their parabolic fits. The 3 σ confidence interval corresponds to ≈ 6 ms.

To carry out the search, the *Ulysses* real-time count rates are extracted for the crossing window and plotted. The data are searched both automatically and by eye. In the automatic procedure, the background count rate is typically calculated over 10 time intervals, and a greater than 4 σ increase is searched for over two or more consecutive time intervals. The search by eye confirms the presence of the increase, and in some cases it identifies increases that were not detected in the automatic procedure due to, for example, a long rise time. If the burst is intense enough to trigger the *Ulysses* GRB detector, burst detection is usually immediately apparent in both the real-time and the triggered data streams, with one noteworthy exception. Very short bursts (durations less than 0.25 s) can trigger, but they remain difficult to identify in the lower time resolution real-time data. Conversely, long bursts that do not reach large peak intensities can be identified in the real-time data but may not trigger, regardless of their time-integrated fluxes.

4. DERIVING ANNULI BY COMPARING BATSE AND *ULYSSES* TIME HISTORIES

When a GRB arrives at two spacecraft with a delay δT, it may be localized to an annulus whose half-angle θ with respect to the vector joining the two spacecraft is given by $\cos\theta = c\delta T/D$, where c is the speed of light and D is the distance between the two spacecraft. (This assumes that the burst is a plane wave, i.e., that its distance is much greater than D.) The annulus width $d\theta$, and thus one dimension of the resulting error box, is $c\sigma(\delta T)/D \sin\theta$, where $\sigma(\delta T)$ is the uncertainty in the time delay. This term has two components, one statistical and one systematic. The first is associated with the uncertainty in comparing the time histories of a burst recorded by two different instruments; the second is due to the uncertainty in the clock calibrations of the two spacecraft. A third source of error is the uncertainty in the knowledge of the spacecraft positions. We discuss each in turn.

In the simple case of identical detectors with identical backgrounds, the most probable delay, δT, and its error, $\sigma(\delta T)$, may be estimated as follows. Denote the two background-subtracted time histories by X_i, Y_i, $i = 1, \ldots, m$; that is, X_1 is the number of counts in the first time bin for detector X, and Y_1 is the number of counts in the first time bin for detector Y, and so on. Assume that the background can be estimated with arbitrary accuracy, and that each value of X_i and Y_i is an independent normal random variable with variance X_i and Y_i, respectively. For simplicity of notation, assume that the two time histories recorded by detectors X and Y are perfectly aligned when time bin 1 of detector X corresponds to time bin 1 of detector Y. Then for this perfect alignment, which corresponds to zero lag between the two time histories, the quantity $R_i = (X_i - Y_i)/(X_i + Y_i)^{1/2}$ is a random variable with mean zero and variance unity for every i. Thus

$$\sum_{i=1}^{n} R_i^2 \tag{1}$$

is distributed as χ^2 with n degrees of freedom. Here the sum is performed over some number n of time bins, where $n \leq m$. Now allow the lag to vary slightly about zero, so that time bin i of detector X corresponds to time bin j of detector Y, and form the random variable $R_{ij} = (X_i - Y_j)/(X_i + Y_j)^{1/2}$, where the lag ij is now variable. The quantity

$$r_{ij}^2 = \sum R_{ij}^2 , \tag{2}$$

where the summation is over the intervals that X and Y have in common, is similarly distributed as χ^2. In practice we do not know a priori the lag at which the best correlation will occur, so we test various lags ij until r_{ij}^2 reaches a minimum, $r_{\min}^2$. Then the lag or time delay corresponding to a 3 σ equivalent confidence level is $r_{ij}^2 = r_{\min}^2 + 9$. (All annuli in this catalog have widths corresponding to 3 σ equivalent confidence.)

Although this simple example describes the essential features of the method, there are numerous complicating factors in practice. For BATSE, the background varies over the orbit, and its value may not always be known accurately; the assumption of a normal distribution may also be violated when Cyg X-1 is in the field of view. The BATSE and *Ulysses* detectors have different areas, burst and background count rates, and time resolutions. We treat this by first normalizing the BATSE background-subtracted time history to the *Ulysses* one so that two time histories have the same total number of counts. We also generate a BATSE time history with identical time resolution to the *Ulysses* one by scaling the counts in the original BATSE time bins. These adjustments complicate the above expressions considerably. However, through Monte Carlo simulations, as well as time history comparisons using a completely different method (Laros et al. 1998), we have verified that the procedure gives correct results. In addition to calculating the r_{ij}^2 statistic, we also compute the correlation coefficient as a function of lag, namely

$$\rho_{ij} = \frac{\sum (X_i - \langle X\rangle)(Y_j - \langle Y\rangle)}{[\sum (X_i - \langle X\rangle)^2 \sum (Y_i - \langle Y\rangle)^2]^{0.5}} ,$$

where the summations are over the intervals that X and Y have in common, and we find its maximum value. The purpose of this calculation is to assure that the r_{ij}^2 statistic has indeed identified the best lag; we require that the maximum ρ_{ij} and the minimum r_{ij}^2 correspond to identical

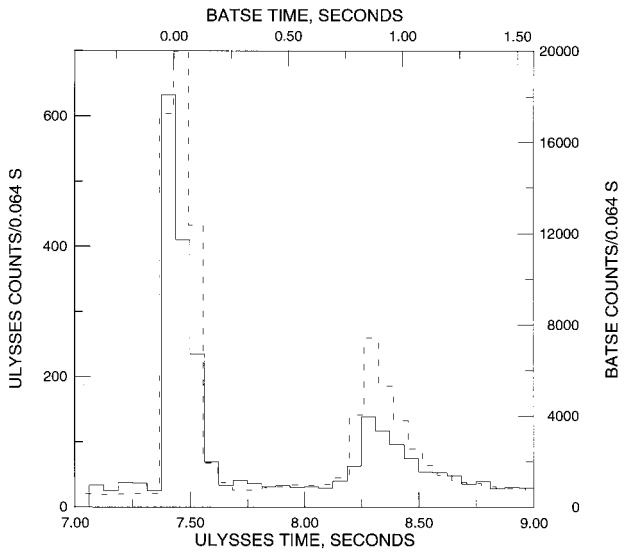

FIG. 4.—*Ulysses* (*solid line*) and BATSE (*dashed line*) time histories aligned for the best fit for the burst of Fig. 1. The BATSE data are summed over four LADs and are not corrected for dead time.

lags, or at worst, that the difference between the lags be much less than the 3 σ confidence interval. Finally, parabolic fits are done to both statistics to identify the best lag and the confidence intervals. An example is shown in Figures 3 and 4.

The second uncertainty, due to the clock calibrations, is in principle much smaller than the 3 σ confidence interval. The clock on the *CGRO* is accurate to 100 μs, and this accuracy is verified through pulsar timing. Onboard software increases the uncertainty in the BATSE trigger times to $\approx$1 ms. The clock on the *Ulysses* spacecraft is calibrated during each daily tracking pass, and the clock drift is extrapolated until the next pass to obtain the correct time; the calibration is verified at 6 month intervals by sending commands to the GRB experiment at precisely known times. The exact procedure is described in Hurley (1994).

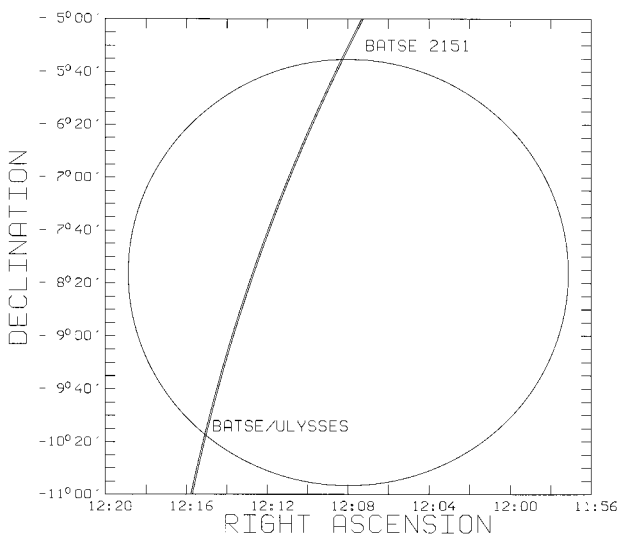

FIG. 5.—*Ulysses*/BATSE triangulation annulus for the burst of Fig. 1, and the BATSE error circle.

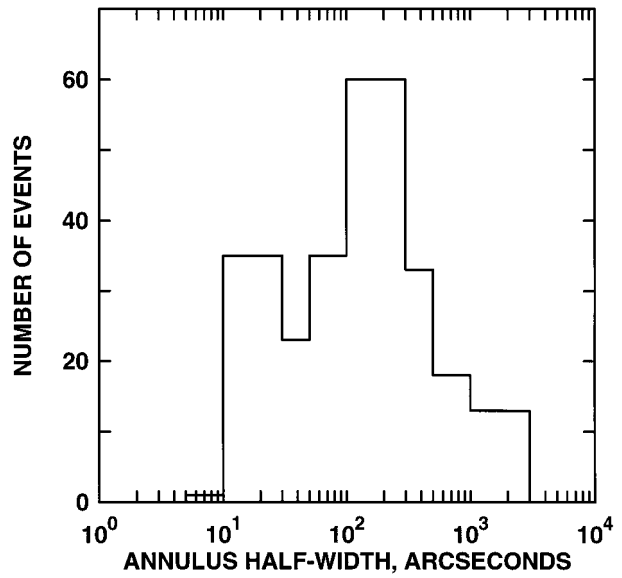

FIG. 6.—Distribution of 218 *Ulysses*/BATSE annulus half-widths (i.e., $\delta R_{\rm IPN}$ in Table 1).

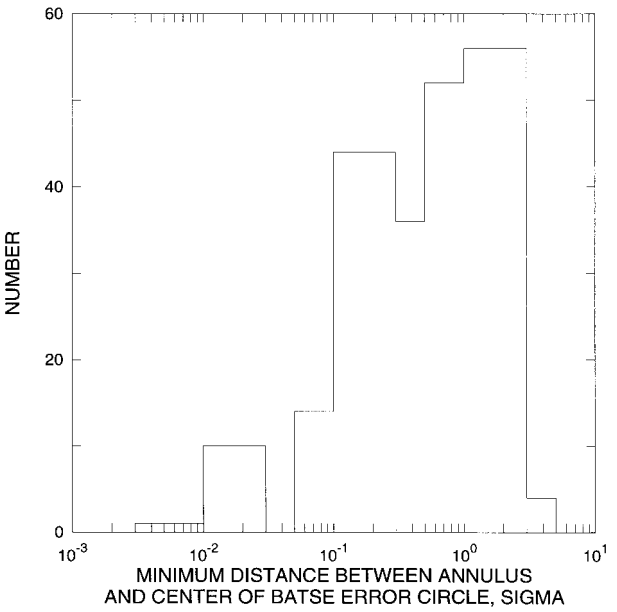

FIG. 7.—Distribution of minimum angular distances between the 218 annuli and the centers of the BATSE error circles. The angular distances are expressed in number of sigma for the BATSE error circle radii, i.e., $d/r_{1\sigma}$.

Due to spacecraft buffering of the commands, the result is that *if* it can be assumed that no errors larger than 125 ms are present, *then* the clock can be shown to be accurate to several milliseconds. For the purposes of triangulation, however, we take the extremely conservative approach that no 3 σ cross-correlation uncertainty is less than 125 ms. Larger timing errors have been identified in the past for both missions. The *CGRO* clock was found to have a consistent 2 s offset in the early part of the mission, and random timing errors between 0.25 and several hundred seconds occurred in certain types of *Ulysses* data. In all cases the data were reprocessed to obtain the results in this paper.

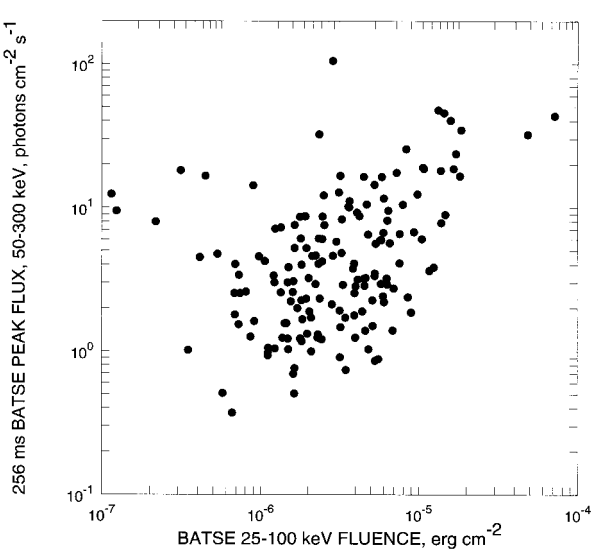

FIG. 8.—Peak fluxes (measured over 256 ms, 50–300 keV) and 25–100 keV fluences of 162 of the bursts in this catalog. No entries are given in the 3B catalog for 56 of the bursts.

Finally, the uncertainties in the spacecraft ephemerides are truly negligible. The *Ulysses* range is known to ≈ 10 km, and the right ascension and declination of the spacecraft are accurate to $\approx 0\overset{\circ}{.}00003$. The *CGRO* range is known to better than 50 km, and the right ascension and declination to better than $0\overset{\circ}{.}01$. The error that these uncertainties produce in the knowledge of the interspacecraft vector (i.e., the center of the annulus) is of order $0\overset{\circ}{.}0005$, and therefore usually 2 orders of magnitude smaller than the timing uncertainties. As a conservative measure, this uncertainty is added linearly to the uncertainties in the annulus parameters caused by the timing. It typically increases the annulus width by several tenths of an arcsecond.

The radius of each annulus and its right ascension and declination are transformed to a heliocentric frame. This is equivalent to an aberration correction (maximum value $\approx 20''$) and involves two adjustments. The first is to the spacecraft time. The signal from a distant spacecraft may travel several thousand seconds on its way to Earth. Depending on the Earth's velocity vector relative to the spacecraft, the relative motion of the Earth and the spacecraft may not be negligible during this period. "Geocentric" clock times are related to the position of the Earth when the signal is *received* from the spacecraft. "Heliocentric" clock times, i.e., times related to the position of the Earth when the signal was *transmitted*, must be used. The difference between the two may be as large as several hundred milliseconds and is often comparable to or greater than the statistical uncertainty of the time history comparison. The second adjustment is to the interspacecraft vector. Two observers moving with the Earth and with the Sun see different vectors (i.e., annulus centers) as a result of their motions during the burst's transit time between the two spacecraft. This correction, too, may not be negligible. The result of triangulating the 1993 January 31 burst is shown in Figure 5.

Although there have never been more than three widely separated spacecraft in the third Interplanetary Network (IPN), which would have provided redundant determinations and therefore a verification of burst positions, there have been numerous instances where a burst source with a known position was triangulated with *Ulysses*, BATSE, and other spacecraft. These include the soft gamma repeater SGR 1806−20 and the bursting pulsar GRO J1744−28 (Hurley et al. 1996, 1998a), the 1997 January 11 burst localized by *BeppoSAX* (Galama et al. 1997), the 1997 February 28 burst with both a *BeppoSAX* location and an optical transient (Hurley et al. 1997c), and numerous other *BeppoSAX* bursts (see, e.g., Hurley et al. 1998b). In each case the triangulated position was in good agreement with the known position of the source.

5. BURST SELECTION CRITERIA

We have used several selection criteria for the bursts in this catalog. The first is that the burst must have been detected by *Ulysses* and BATSE. Because of the very different detector sizes, all of the bursts satisfying this criterion are observed to be rather intense by BATSE, and therefore detection by BATSE is unambiguous. However, the weaker events (as observed by *Ulysses* in the real-time mode) may be difficult to identify. In these cases, we rely on several supplementary semiempirical criteria. One is that the $r^2_{\rm min}$ statistic, divided by the number of degrees of freedom, be less than unity. Another is that the maximum value of the correlation coefficient ρ be greater than 0.5. Yet another is that the ratio of *Ulysses* counts to BATSE counts lie in the range 0.019 ± 0.009. It might seem unusual that the average value of this ratio is 0.019, whereas the ratio of the *Ulysses* projected area in any direction to a single BATSE LAD area is closer to 0.01, and the BATSE counts are derived from at least two LADs in this procedure. Several factors account for this. First, the *Ulysses* energy range is wider than that of BATSE: 25–150 versus 25–100 keV. Second, the *Ulysses* lower energy threshold actually allows photons with energies as low as 15 keV to be counted, albeit with lower efficiency. Third, the two *Ulysses* hemispherical detectors are thin, so photons that do not interact in one hemisphere may interact in the other, increasing the effective area. Finally, the BATSE count rates are not corrected for dead time, which is known to affect the brighter bursts and are, in general, among the bursts we observe.

This set of criteria is not an absolute one. To a good approximation, every GRB is different from every other one. In addition, data gaps, Earth occultation, telemetry noise, unusual background behavior, and different data modes complicate some analyses. In some cases, bursts satisfying all the criteria above are rejected because they are simply too weak to allow reliable triangulation. In other cases, bursts that do not satisfy one or more criteria may be accepted.

A final criterion for inclusion in this catalog is that the burst must not have been observed by a third interplanetary spacecraft. The *Ulysses* BATSE bursts also observed by *Mars Observer* have been published in Laros et al. (1997). The *Ulysses* BATSE bursts also observed by *Pioneer Venus Orbiter* are in Laros et al. (1998).

6. A FEW STATISTICS

Over the period covered by the 3B catalog, *Ulysses* observed 346 confirmed cosmic GRBs (i.e., bursts that were observed by at least one other spacecraft). Of these, 274 were observed by *Ulysses* and BATSE, and in some cases by other spacecraft as well.[2] Since BATSE observed 1122 bursts during this period, *Ulysses* observed approximately one out of every four BATSE bursts. Of the 274 bursts, 64 were observed by *Ulysses* in triggered mode, and 210 were observed in real-time mode. Finally, 220 were observed by *Ulysses* and BATSE, but not by a third interplanetary spacecraft; two of these could not be triangulated according to the criteria explained above.

The histogram of Figure 6 shows the distribution of annulus half-widths for the 218 bursts localized. The smallest is about $7''$, the largest is $32'$, and the average is $4\overset{'}{.}5$; 158 of the annuli, or 72%, intersect the BATSE 1 σ error circles whose radii are defined by $r_{1\sigma} = (\sigma^2_{\rm stat} + \sigma^2_{\rm sys})^{1/2}$, where $\sigma_{\rm sys}$ is the systematic error, $1\overset{\circ}{.}6$, and $\sigma_{\rm stat}$ is the statistical error. Figure 5 shows one example. This is less than the number that would have been predicted (87%). An analysis of a preliminary version of the IPN catalog describes several more complicated BATSE error models that are consistent with the BATSE IPN separations (Briggs et al. 1998b). A more extensive analysis, which utilizes the *Ulysses* supplement to the 4B catalog, is in progress (Briggs et al. 1998a).

[2] A list of all cosmic bursts and the spacecraft that detected them may be found at http://ssl.berkeley.edu/ipn3/index.html.

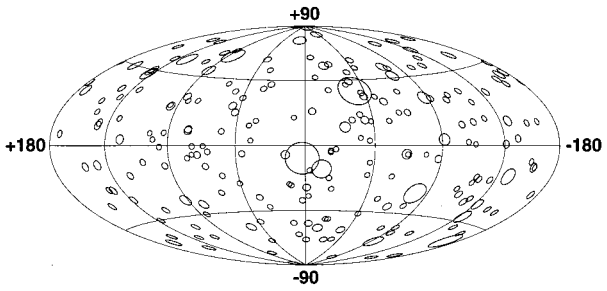

FIG. 9.—Distribution of 218 BATSE 3B error circles in galactic coordinates.

One quantity of interest is how close the annulus passes to the center of the error circle. Let α_1, δ_1 be the right ascension and declination of the center of a BATSE error circle, respectively, and let α_2, δ_2, θ_2 be the right ascension, declination, and radius of an annulus, respectively. Then the minimum distance between the error circle and the annulus is given by $d = |\theta_2 - \cos^{-1}[\sin(\delta_1)\sin(\delta_2) + \cos(\delta_1)\cos(\delta_2)\sin(\alpha_1 - \alpha_2)]|$. A histogram of the distribution of minimum distances between the annuli and the centers of the BATSE error circles is given in Figure 7.

In general, the annuli obtained by triangulations are small circles on the celestial sphere, so their curvature, even across a relatively small BATSE error circle, is not always negligible, and a simple four-sided error box cannot be defined. This curvature can be seen in Figure 5. For this reason, we do not cite the intersection points of the annulus with the error circle. However, we give here the formulas for finding these points for those cases where it may be useful. Let α_1, δ_1, θ_1 and α_2, δ_2, θ_2 be the right ascension, declination, and radii of the two small circles. Let α, δ be the right ascension and declination of the intersection points.

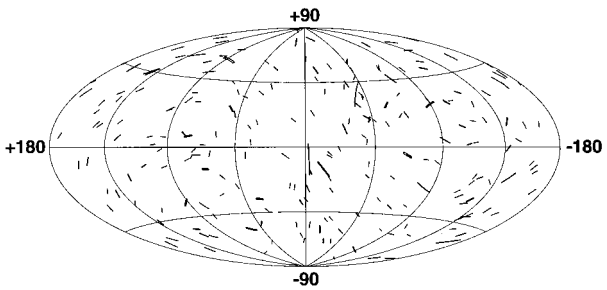

FIG. 10.—Distribution of 218 *Ulysses*/BATSE error circle/annulus intersections.

TABLE 1

COMPLETENESS ABOVE VARIOUS THRESHOLDS

BATSE Threshold	Approximate Completeness (lower limit)
1.8×10^{-9} ergs cm^{-2}	0.25
$\times 10^{-6}$ ergs cm^{-2}	0.49
$\times 10^{-5}$ ergs cm^{-2}	0.74
0.27 photons cm^{-2} s^{-1}	0.25
1 photon cm^{-2} s^{-1}	0.34
10 photons cm^{-2} s^{-1}	0.65

Then $\sin\delta = [-b \pm (b^2 - 4ac)^{1/2}]/2a$, where

$$a = -\cos^2\delta_1\cos^2\delta_2\sin^2(\alpha_1 - \alpha_2) + 2\sin\delta_1\sin\delta_2\cos\delta_1\cos\delta_2\cos(\alpha_1 - \alpha_2), - \sin^2\delta_2\cos^2\delta_1 - \sin^2\delta_1\cos^2\delta_2,$$

$$b = -2(\cos\theta_1\sin\delta_2 + \cos\theta_2\sin\delta_1) \times \cos\delta_1\cos\delta_2\cos(\alpha_1 - \alpha_2), + 2\cos\theta_2\sin\delta_2\cos^2\delta_1 + 2\cos\theta_1\sin\delta_1\cos^2\delta_2,$$

and

$$c = \cos^2\delta_1\cos^2\delta_2\sin^2(\alpha_1 - \alpha_2) + 2\cos\theta_2\cos\theta_1\cos\delta_1\cos\delta_2\cos(\alpha_1 - \alpha_2), - \cos^2\theta_2\cos^2\delta_1 - \cos^2\theta_1\cos^2\delta_2.$$

For each of the two values of the declination δ, the corresponding right ascension α is given by

$$\alpha = \alpha_1 + \cos^{-1}[(\cos\theta_1 - \sin\delta\sin\delta_1)/\cos\delta\cos\delta_1].$$

Figure 8 shows the BATSE peak fluxes and fluences for 162 of the 218 bursts with flux and fluence entries in the 3B catalog. There is a slight tendency for some of the smaller fluence events to have relatively large peak fluxes over a time interval comparable to that of the *Ulysses* real-time data, which helps to explain why these bursts were detected by *Ulysses*. To estimate the completeness of this catalog, we have calculated the ratios of the number of bursts detected by *Ulysses* to the number detected by BATSE above several flux and fluence thresholds, starting with the weakest events in the BATSE catalog; we have used the 25–100 keV fluences in ergs cm^{-2} and the peak 25–300 keV fluxes over 256 ms in photons cm^{-2} s^{-1}. Since events detected by a third spacecraft are not included in the present catalog, the numbers given represent lower limits to the completeness. Table 1 summarizes the results.

Finally, we have analyzed these annuli for intersections that might provide evidence of repeating bursts from a single source. Although there was a large, but statistically insignificant, number of two annulus intersections, we found only one case where a three-way intersection almost occurred (BATSE bursts 451, 2286, and 2619); the data are therefore consistent with no burst repetition.

7. TABLE OF ANNULI

Table 2 supercedes previous lists that have been circulated in the past, but have not been published. The changes to it include the following: (1) the use of final time history and spacecraft ephemeris data—earlier lists often used preliminary and predict data with correspondingly larger timing uncertainties; (2) transformation of annuli to heliocentric coordinates—earlier lists often gave geocentric coordinates, with correspondingly larger uncertainties in the annulus widths; (3) removal of weak events according to the criteria in § 5; (4) reprocessing of data to eliminate known clock errors; and (5) careful examination of bursts whose BATSE time histories were truncated by data gaps and Earth occultation.

Figures 9 and 10 compare the BATSE error circles with the IPN annulus/error circle intersections for the bursts in

TABLE 2

Ulysses/BATSE ANNULI

Date (1)	UT (2)	N_B (3)	$\alpha_{2000,B}$ (4)	$\delta_{2000,B}$ (5)	$\sigma_{\mathrm{stat},B}$ (6)	$\alpha_{2000,\mathrm{IPN}}$ (7)	$\delta_{2000,\mathrm{IPN}}$ (8)	R_{IPN} (9)	δR_{IPN} (10)
91 Apr 25	00:37:46	109	91.29	−22.77	1.02	115.140	23.171	51.784	0.051
91 Apr 29	03:11:50	121	174.75	14.33	1.36	116.426	22.919	59.157	0.136
91 May 02.....	22:37:23	142	46.22	−52.71	0.62	297.624	−22.677	87.126	0.023
91 May 03.....	07:04:13	143	87.45	38.74	0.87	117.731	22.655	30.360	0.009
91 May 11.....	02:11:48	179	266.48	58.30	1.66	300.193	−22.137	83.666	0.018
91 May 23.....	19:03:25	222	106.99	0.36	1.28	124.202	21.228	26.847	0.051
91 Jun 01.....	19:22:14	249	310.12	32.34	0.17	307.035	−20.537	52.942	0.008
91 Jun 02.....	22:55:01	257	142.76	53.99	2.06	127.387	20.448	34.526	0.163
91 Jun 26.....	07:15:13	444	133.38	7.72	1.27	134.557	18.501	10.164	0.020
91 Jun 30.....	07:37:02	469	304.70	35.13	0.91	315.764	−18.148	52.439	0.085
91 Jul 21.....	19:30:12	563	315.52	−14.29	1.31	322.022	−16.198	6.769	0.436
91 Aug 09	06:15:00	659	195.43	19.37	1.85	147.088	14.483	50.860	0.092
91 Aug 09	19:35:45	660	281.96	64.74	2.01	327.238	−14.431	85.747	0.016
91 Sep 05.....	23:48:55	761	360.00	−81.05	0.82	334.075	−11.942	70.787	0.017
91 Sep 07.....	01:05:23	764	136.55	−28.23	1.30	154.322	11.849	43.573	0.131
91 Sep 26.....	18:25:57	824	346.07	21.36	2.70	338.688	−10.171	32.155	0.294
91 Sep 27.....	23:26:53	829	50.16	−39.65	0.34	338.937	−10.074	68.870	0.036
91 Sep 30.....	11:55:30	841	131.80	−20.62	1.27	159.447	9.874	39.201	0.013
91 Sep 06.....	09:01:54	871	33.30	−45.44	3.38	340.603	−9.419	50.544	0.087
91 Oct 22.....	04:13:58	914	123.91	70.34	1.03	163.395	8.312	68.583	0.017
91 Oct 26.....	13:07:01	938	74.68	−22.27	2.40	344.080	−8.038	80.644	0.068
91 Nov 06.....	03:42:01	1008	343.03	−35.16	0.83	345.570	−7.445	29.223	0.023
91 Nov 23.....	08:15:33	1114	22.81	30.34	1.14	347.386	−6.730	49.421	0.015
91 Nov 27.....	04:22:08	1122	269.14	49.73	0.38	347.680	−6.617	88.466	0.005
91 Dec 07	09:50:45	1150	307.79	29.30	1.59	348.248	−6.408	53.876	0.059
91 Dec 09	18:35:58	1157	259.98	−45.08	0.40	348.333	−6.380	82.576	0.003
91 Dec 17	08:22:06	1190	6.96	22.67	1.02	348.480	−6.340	35.915	0.032
91 Dec 21	22:03:26	1200	215.82	−42.72	1.98	168.475	6.356	61.764	0.111
91 Dec 24	11:02:58	1212	45.43	−10.79	4.68	348.444	−6.377	57.290	0.117
91 Dec 27	01:05:53	1235	350.44	−68.25	0.67	348.389	−6.408	61.852	0.064
92 Jan 10.....	09:17:58	1288	58.08	−20.80	0.42	347.700	−6.748	69.190	0.018
92 Feb 21	06:14:32	1425	184.14	48.48	0.65	161.368	8.446	42.142	0.008
92 Feb 24	02:43:39	1432	169.65	−66.78	2.73	160.726	8.515	75.175	0.539
92 Feb 27	06:00:51	1443	68.36	66.84	1.33	160.016	8.591	83.353	0.005
92 Mar 07.....	00:18:04	1467	355.57	−45.15	1.16	338.049	−8.795	39.316	0.066
92 Mar 15.....	04:19:27	1484	320.58	−20.89	0.46	336.280	−8.960	16.873	0.013
92 Apr 07	12:03:40	1543	341.44	−10.68	2.04	332.036	−9.187	9.927	0.437
92 Apr 08	12:05:56	1545	138.96	40.83	0.58	151.890	9.190	34.380	0.022
92 Apr 29	18:59:32	1571	179.08	−14.33	2.85	149.602	8.963	39.318	0.091
92 May 02.....	06:02:59	1577	33.05	−17.73	1.04	329.440	−8.908	60.781	0.026
92 May 13.....	16:52:39	1606	211.16	−44.77	0.65	148.956	8.591	74.250	0.005
92 May 30.....	22:59:55	1630	162.68	18.13	1.67	148.993	7.901	17.618	0.070
92 Jun 17.....	05:26:51	1652	37.66	77.51	0.51	149.807	6.977	89.064	0.012
92 Jun 22.....	07:05:05	1663	162.10	47.17	0.31	150.169	6.667	41.336	0.005
92 Jun 22.....	12:54:21	1664	346.81	10.01	0.55	330.187	−6.649	18.892	0.018
92 Jun 27.....	13:02:36	1676	166.02	−2.58	0.65	150.593	6.327	23.504	0.017
92 Jul 01.....	19:38:19	1683	314.64	33.44	0.63	330.973	−6.033	42.560	0.017
92 Jul 14.....	20:23:26	1700	140.36	−44.64	3.28	152.298	5.079	50.262	0.099
92 Jul 18.....	14:40:36	1708	22.44	−3.98	1.14	332.718	−4.782	49.196	0.032
92 Jul 18.....	21:32:43	1709	296.39	−55.98	0.48	332.751	−4.760	58.948	0.004
92 Jul 21.....	18:17:48	1717	37.55	33.49	0.73	333.083	−4.530	72.485	0.033
92 Jul 23.....	01:00:34	1721	85.79	7.78	0.48	153.234	4.427	68.971	0.008
92 Aug 01	01:16:40	1733	157.86	68.90	1.12	154.338	3.667	64.462	0.021
92 Aug 13	03:33:48	1807	206.22	−28.34	1.75	155.907	2.581	63.921	0.051
92 Aug 14	06:09:53	1815	258.68	−44.63	0.79	336.053	−2.478	78.143	0.006
92 Aug 24	10:53:03	1872	228.59	−51.79	0.33	157.427	1.505	76.788	0.003
92 Aug 30	01:45:18	1883	258.53	−73.99	0.54	338.192	−0.949	86.267	0.010
92 Sep 02.....	00:29:05	1886	279.15	−20.70	2.29	338.594	−0.651	61.607	0.015
92 Sep 03.....	00:49:17	1888	61.97	−68.37	0.75	338.732	−0.549	88.165	0.010
92 Sep 25.....	21:45:16	1956	160.26	67.38	1.34	161.773	−1.864	68.233	0.020
92 Sep 03.....	06:35:40	1974	150.32	−14.71	0.55	162.694	−2.674	19.765	0.021
92 Sep 09.....	06:41:11	1983	120.41	−29.10	0.39	163.411	−3.345	46.240	0.003
92 Oct 15.....	01:36:32	1989	123.04	41.69	0.95	164.066	−3.998	57.677	0.040
92 Oct 22.....	15:20:59	1997	253.78	−12.42	0.41	164.862	−4.861	88.377	0.002

TABLE 2—*Continued*

Date (1)	UT (2)	N_B (3)	$\alpha_{2000,B}$ (4)	$\delta_{2000,B}$ (5)	$\sigma_{\mathrm{stat},B}$ (6)	$\alpha_{2000,\mathrm{IPN}}$ (7)	$\delta_{2000,\mathrm{IPN}}$ (8)	R_{IPN} (9)	δR_{IPN} (10)
92 Oct 29.....	12:37:56	2018	34.14	−1.57	1.67	345.514	5.651	50.169	0.045
92 Oct 30.....	01:16:31	2020	86.16	6.86	1.75	165.561	−5.710	79.293	0.042
92 Nov 18.....	22:11:44	2061	350.45	50.32	1.07	346.930	7.990	41.232	0.128
92 Nov 23.....	06:18:31	2067	334.24	−53.25	0.72	347.111	8.481	64.897	0.008
92 Dec 03.....	21:44:22	2074	233.62	21.03	0.74	167.337	−9.664	68.339	0.119
92 Dec 06.....	18:24:19	2080	176.48	45.72	0.77	167.341	−9.975	51.667	0.029
92 Dec 07.....	16:00:48	2083	306.33	−42.93	0.44	347.336	10.074	62.709	0.003
92 Dec 09.....	02:40:56	2089	172.98	61.45	0.51	167.325	−10.228	68.392	0.048
92 Dec 09.....	11:35:38	2090	332.97	−52.02	0.68	347.320	10.269	63.995	0.009
92 Dec 18.....	02:30:02	2102	355.62	−55.31	1.76	347.091	11.168	66.903	0.076
92 Dec 27.....	12:44:08	2106	206.33	−25.65	1.04	166.535	−12.089	39.698	0.113
92 Dec 30.....	08:57:51	2110	19.52	17.21	0.33	346.301	12.353	32.939	0.112
92 Dec 30.....	14:05:46	2111	150.54	28.63	1.71	166.282	−12.370	45.110	0.086
93 Jan 06.....	15:37:39	2121	6.08	2.00	0.53	345.556	12.984	21.048	0.021
93 Jan 06.....	19:57:15	2122	124.79	−32.62	0.68	165.536	−12.996	42.302	0.149
93 Jan 08.....	02:28:55	2123	94.62	−30.44	0.99	165.383	−13.100	65.116	0.069
93 Jan 12.....	03:47:31	2127	226.32	27.74	1.22	164.853	−13.415	72.911	0.021
93 Jan 12.....	15:18:02	2128	210.10	51.92	1.02	164.786	−13.451	76.849	0.066
93 Jan 16.....	02:47:02	2136	246.99	15.91	1.02	164.275	−13.700	88.748	0.026
93 Jan 27.....	16:14:25	2149	310.95	−39.63	1.16	342.242	14.382	60.557	0.155
93 Jan 31.....	18:57:12	2151	182.04	−8.24	2.16	161.406	−14.563	22.249	0.009
93 Feb 01.....	16:41:55	2156	333.53	41.15	1.26	341.214	14.601	27.869	0.023
93 Feb 05.....	10:10:31	2166	278.00	−45.74	5.98	340.403	14.729	83.936	0.277
93 Feb 17.....	14:44:38	2197	117.78	0.98	2.27	157.517	−14.945	41.809	0.234
93 Mar 02.....	21:33:17	2213	90.33	5.43	0.62	154.166	−14.821	66.384	0.016
93 Mar 09.....	03:07:50	2228	325.41	51.73	0.72	332.605	14.648	36.594	0.012
93 Mar 10.....	07:19:20	2232	284.35	−52.39	0.89	332.316	14.607	79.362	0.007
93 Mar 18.....	12:29:53	2255	150.48	−18.85	1.09	150.361	−14.267	5.323	0.320
93 Mar 29.....	03:09:25	2273	179.25	−8.65	0.94	148.090	−13.723	35.582	0.010
93 Mar 31.....	03:11:16	2276	43.00	47.27	2.03	327.701	13.613	77.070	0.078
93 Apr 05.....	08:54:49	2286	198.18	−8.80	0.55	146.754	−13.315	52.136	0.005
93 Apr 06.....	07:16:25	2289	299.81	29.01	0.51	326.595	13.263	31.383	0.011
93 Apr 09.....	04:50:10	2295	295.83	43.18	2.04	326.125	13.098	37.466	0.366
93 Apr 09.....	21:25:40	2297	176.91	−39.75	1.25	146.019	−13.056	39.155	0.088
93 Apr 14.....	02:27:15	2303	311.42	9.92	0.91	325.406	12.819	14.314	0.061
93 Apr 18.....	14:38:18	2307	311.65	21.37	1.27	324.831	12.570	14.596	0.415
93 Apr 24.....	19:19:00	2315	54.22	41.60	1.67	324.179	12.245	86.680	0.134
93 Apr 25.....	10:17:29	2316	18.00	−35.19	0.31	324.122	12.214	70.285	0.034
93 Apr 26.....	12:40:32	2319	67.82	10.13	1.10	144.025	−12.159	75.515	0.028
93 Apr 28.....	01:07:12	2320	129.85	−55.45	1.68	143.900	−12.085	46.202	0.005
93 Apr 30.....	15:01:18	2321	106.33	20.97	0.36	143.709	−11.967	50.803	0.009
93 May 02.....	13:52:52	2323	254.72	−46.53	0.78	323.580	11.882	87.103	0.039
93 May 06.....	14:52:51	2329	64.45	−5.97	0.24	143.364	−11.717	77.827	0.004
93 May 18.....	03:20:25	2346	349.17	−37.51	1.04	323.086	11.354	53.387	0.019
93 May 23.....	19:40:53	2350	14.80	4.21	2.64	323.121	11.238	44.153	0.124
93 May 31.....	15:53:38	2362	340.04	13.25	2.16	323.341	11.152	15.895	0.044
93 Jun 09.....	10:07:24	2383	208.73	−16.38	1.62	143.799	−11.158	64.377	0.132
93 Jun 14.....	03:40:30	2393	168.14	23.95	1.15	144.132	−11.210	42.800	0.008
93 Jul 05.....	12:39:08	2429	283.08	−39.24	0.99	326.244	11.861	65.410	0.124
93 Jul 06.....	08:09:10	2432	210.09	−1.36	1.31	146.342	−11.898	63.498	0.045
93 Jul 08.....	05:12:38	2433	86.55	−69.02	6.25	146.572	−11.989	62.867	0.076
93 Jul 09.....	06:14:22	2436	194.41	−46.73	0.67	146.700	−12.042	54.525	0.028
93 Jul 14.....	16:12:53	2446	257.70	23.70	0.97	327.399	12.344	68.720	0.048
93 Jul 21.....	01:17:22	2452	78.66	−33.15	1.52	148.275	−12.751	66.262	0.085
93 Jul 21.....	12:45:35	2453	298.58	−40.79	1.79	328.342	12.785	61.079	0.101
93 Jul 27.....	08:08:29	2466	159.99	−23.89	1.28	149.185	−13.209	16.546	0.136
93 Jul 31.....	03:16:31	2475	116.53	45.49	2.15	149.754	−13.514	66.345	0.036
93 Aug 05.....	12:39:28	2482	334.55	−15.60	0.83	330.584	13.983	30.305	0.208
93 Aug 09.....	05:11:04	2486	37.97	−74.63	1.79	151.166	−14.323	80.857	0.088
93 Aug 22.....	14:44:51	2500	213.09	−0.68	2.28	153.348	−15.724	65.872	0.232
93 Aug 31.....	09:16:05	2507	223.29	−3.63	0.47	154.815	−16.774	67.536	0.007
93 Sep 03.....	00:19:29	2511	88.67	−10.42	4.20	155.258	−17.109	64.672	0.109
93 Sep 05.....	03:26:30	2514	310.95	−1.22	0.63	335.615	17.389	28.629	0.006
93 Sep 10.....	12:12:08	2522	167.59	−66.69	0.54	156.521	−18.114	48.810	0.044
93 Sep 14.....	02:49:11	2530	34.26	34.29	1.53	337.128	18.628	50.198	0.173

TABLE 2—*Continued*

Date (1)	UT (2)	N_B (3)	$\alpha_{2000,B}$ (4)	$\delta_{2000,B}$ (5)	$\sigma_{\mathrm{stat},B}$ (6)	$\alpha_{2000,\mathrm{IPN}}$ (7)	$\delta_{2000,\mathrm{IPN}}$ (8)	R_{IPN} (9)	δR_{IPN} (10)
93 Sep 16.....	20:19:23	2533	280.71	65.39	0.22	337.586	19.026	57.392	0.013
93 Sep 22.....	06:24:46	2537	271.20	55.89	0.45	338.488	19.847	67.999	0.003
93 Sep 27.....	04:18:07	2542	108.61	−9.52	1.62	159.296	−20.624	52.084	0.115
93 Oct 06.....	21:31:50	2566	66.31	65.28	1.70	340.850	22.262	70.461	0.049
93 Oct 08.....	07:18:14	2570	42.98	21.37	0.85	341.069	22.510	58.202	0.082
93 Oct 08.....	11:09:10	2571	165.40	33.93	0.86	161.094	−22.537	60.104	0.027
93 Oct 14.....	17:01:01	2586	272.50	9.34	0.50	342.042	23.672	67.956	0.010
93 Oct 17.....	01:17:49	2590	181.44	−83.11	0.65	162.389	−24.110	58.979	0.003
93 Oct 19.....	18:22:34	2593	242.92	−18.70	1.66	162.779	−24.628	73.476	0.025
93 Oct 24.....	13:29:09	2603	137.63	−8.49	0.53	163.447	−25.567	30.574	0.083
93 Oct 26.....	11:35:57	2606	51.36	−10.56	0.48	343.704	25.955	75.482	0.087
93 Oct 30.....	08:08:42	2609	326.41	58.24	0.55	344.202	26.745	31.863	0.058
93 Oct 31.....	04:06:35	2611	325.10	62.73	0.32	344.306	26.918	37.073	0.005
93 Nov 03.....	16:25:42	2617	87.88	65.05	0.31	344.732	27.657	72.278	0.008
93 Nov 06.....	20:32:04	2619	196.75	−3.13	1.11	165.094	−28.337	40.406	0.232
93 Nov 12.....	18:45:53	2628	311.51	55.95	0.53	345.711	29.654	34.291	0.010
93 Nov 26.....	04:46:46	2660	157.28	70.08	3.02	346.750	32.795	80.134	0.109
93 Nov 26.....	19:31:39	2661	3.29	−17.40	0.22	346.785	32.945	50.498	0.004
93 Dec 04.....	09:48:10	2676	250.15	38.23	0.18	347.083	34.824	76.909	0.004
93 Dec 05.....	14:59:51	2679	15.56	66.49	2.22	347.108	35.133	38.364	0.018
93 Dec 08.....	04:37:19	2682	198.73	−29.93	0.56	167.142	−35.783	34.384	0.050
93 Dec 08.....	09:34:40	2683	234.11	−40.29	3.06	167.143	−35.836	51.960	0.143
93 Dec 21.....	02:09:50	2700	91.02	−43.17	0.50	166.799	−39.143	56.073	0.036
93 Dec 22.....	21:21:33	2703	192.52	28.65	0.66	166.675	−39.621	73.261	0.251
93 Dec 25.....	23:20:12	2709	4.85	9.87	0.79	346.415	40.440	35.141	0.212
93 Dec 26.....	20:11:09	2711	205.95	21.63	2.82	166.329	−40.669	74.178	0.127
94 Jan 01.....	22:42:00	2729	189.27	62.84	3.47	345.578	42.289	78.226	0.064
94 Jan 02.....	02:45:52	2732	10.90	45.11	1.27	345.554	42.335	18.951	0.195
94 Jan 03.....	22:12:56	2736	267.90	7.14	0.65	345.274	42.810	76.721	0.016
94 Jan 13.....	16:47:54	2756	209.39	−23.16	9.65	163.289	−45.332	42.651	0.049
94 Jan 19.....	15:44:40	2773	131.41	39.29	1.39	161.654	−46.793	89.606	0.051
94 Jan 28.....	16:50:58	2790	224.02	−15.22	0.96	158.510	−48.816	64.647	0.059
94 Jan 29.....	10:43:17	2793	127.46	28.59	0.82	158.217	−48.971	81.612	0.072
94 Feb 01.....	07:40:40	2794	268.61	22.37	1.67	337.027	49.542	59.277	0.125
94 Feb 03.....	15:46:56	2797	184.16	−40.95	0.58	156.002	−49.973	20.512	0.052
94 Feb 06.....	00:08:37	2798	144.20	−59.96	0.15	154.922	−50.380	13.687	0.039
94 Feb 10.....	19:13:16	2812	152.29	82.13	0.66	332.566	51.121	48.298	0.007
94 Feb 17.....	23:02:42	2831	29.07	4.55	0.69	328.739	51.947	69.334	0.005
94 Feb 18.....	19:32:28	2833	349.71	−19.69	0.35	328.264	52.023	73.939	0.010
94 Feb 28.....	11:29:00	2852	127.98	−12.36	0.44	142.713	−52.495	42.173	0.012
94 Mar 01.....	20:10:37	2855	103.51	64.35	0.35	321.919	52.509	59.400	0.029
94 Mar 02.....	05:08:31	2856	12.49	−23.97	0.21	321.700	52.508	88.572	0.005
94 Mar 12.....	11:28:22	2877	221.50	−56.17	0.61	135.895	−52.124	48.964	0.052
94 Mar 19.....	23:57:20	2889	68.74	−12.60	0.39	132.014	−51.403	62.552	0.090
94 Mar 21.....	22:05:07	2890	160.33	3.10	0.85	131.093	−51.168	58.918	0.233
94 Mar 23.....	22:04:38	2891	213.89	8.37	0.85	310.173	50.907	85.032	0.016
94 Mar 28.....	12:05:34	2894	97.18	−32.35	0.58	128.216	−50.236	26.692	0.028
94 Mar 29.....	05:49:26	2895	237.51	−68.89	0.50	127.917	−50.121	51.112	0.006
94 Mar 29.....	18:15:37	2897	204.91	−10.33	1.00	127.712	−50.040	69.434	0.026
94 Mar 30.....	20:44:39	2899	193.80	−33.63	1.72	127.286	−49.861	48.714	0.320
94 Apr 06.....	01:10:54	2913	225.44	−39.10	1.24	125.133	−48.806	69.435	0.043
94 Apr 10.....	15:45:02	2919	254.89	30.80	0.93	303.788	47.974	42.261	0.047
94 Apr 12.....	01:40:31	2922	217.17	−38.35	1.12	123.422	−47.710	58.846	0.303
94 Apr 14.....	16:46:25	2929	181.26	−26.15	0.50	122.794	−47.222	49.154	0.026
94 Apr 19.....	19:10:58	2940	359.86	−47.95	0.58	121.768	−46.270	73.314	0.062
94 Apr 29.....	00:43:53	2953	35.10	−57.52	0.32	120.524	−44.594	51.727	0.006
94 May 03.....	05:07:44	2958	161.00	10.06	0.60	120.195	−43.873	64.039	0.057
94 May 12.....	17:37:50	2974	232.97	55.88	2.65	299.935	42.376	44.482	0.007
94 May 20.....	00:21:38	2984	323.50	6.93	0.88	300.146	41.389	40.428	0.019
94 May 26.....	10:55:26	2993	80.41	−30.39	0.96	120.590	−40.650	33.571	0.347
94 May 26.....	20:20:05	2994	131.85	34.20	1.69	120.622	−40.611	76.690	0.012
94 May 29.....	03:17:02	2998	163.64	−25.33	3.45	120.834	−40.382	35.002	0.334
94 May 29.....	16:20:36	3002	66.19	−23.75	3.30	120.889	−40.330	47.443	0.021
94 May 29.....	21:18:56	3003	214.84	58.93	0.46	300.908	40.314	56.125	0.083
94 Jun 09.....	16:29:06	3024	284.14	23.34	1.01	302.269	39.513	18.866	0.118

TABLE 2—*Continued*

Date (1)	UT (2)	N_B (3)	$\alpha_{2000,B}$ (4)	$\delta_{2000,B}$ (5)	$\sigma_{\mathrm{stat},B}$ (6)	$\alpha_{2000,\mathrm{IPN}}$ (7)	$\delta_{2000,\mathrm{IPN}}$ (8)	R_{IPN} (9)	δR_{IPN} (10)
94 Jun 19	21:31:20	3035	299.05	−29.89	0.34	303.996	39.141	69.575	0.026
94 Jun 22	13:18:16	3039	299.58	−31.24	0.82	304.505	39.108	72.495	0.012
94 Jun 23	18:46:23	3042	108.37	75.78	0.46	304.747	39.101	65.666	0.013
94 Jul 01	21:46:38	3055	145.18	−6.43	0.81	126.479	−39.199	37.139	0.157
94 Jul 02	09:28:11	3056	29.73	−23.53	0.57	126.586	−39.214	78.876	0.116
94 Jul 03	04:40:46	3057	131.50	27.39	1.25	126.771	−39.239	67.508	0.005
94 Jul 04	23:32:07	3060	212.49	47.25	0.64	307.181	39.305	67.688	0.082
94 Jul 06	19:24:33	3062	265.11	26.40	1.86	307.614	39.384	36.694	0.287
94 Jul 08	20:42:06	3067	301.58	24.66	1.02	308.112	39.490	17.427	0.022
94 Jul 14	12:54:21	3075	333.58	−42.10	1.59	309.555	39.862	85.495	0.067
94 Jul 17	03:24:29	3087	109.80	12.93	0.71	130.246	−40.076	54.328	0.006
94 Jul 28	02:55:32	3099	42.57	−49.08	0.76	133.354	−41.280	60.269	0.045
94 Jul 28	14:06:40	3100	291.22	4.45	1.29	313.491	41.344	44.189	0.181
94 Jul 28	23:58:54	3101	85.49	−39.87	1.44	133.620	−41.397	36.263	0.066
94 Aug 06.....	04:38:48	3108	276.21	−31.33	10.69	316.177	42.651	86.962	0.079
94 Aug 06.....	09:32:56	3109	242.38	13.65	1.22	316.242	42.686	69.105	0.126
94 Aug 10.....	02:22:42	3115	212.01	−17.47	0.53	137.468	−43.347	67.696	0.009
94 Aug 12.....	00:27:42	3119	340.49	−46.12	2.23	138.120	−43.715	86.692	0.263
94 Aug 17.....	08:40:15	3128	280.84	3.47	0.40	319.994	44.823	53.907	0.010
94 Aug 21.....	21:51:27	3131	294.69	43.48	1.77	321.670	45.864	16.142	0.191
94 Aug 26.....	20:55:20	3138	93.59	−34.63	0.45	143.593	−47.103	37.845	0.013
94 Aug 30.....	08:59:56	3143	193.66	25.66	1.58	145.011	−48.048	89.313	0.042
94 Sep 10	19:31:24	3163	332.01	−34.11	0.94	330.099	51.525	87.032	0.065
94 Sep 15	06:52:19	3168	219.42	47.70	4.53	332.318	53.052	62.836	0.393

NOTE.—Col. (1) is the date of the burst; col. (2) is the Universal Time of the burst at Earth; col. (3) is the BATSE number for the burst; col. (4) is the BATSE right ascension of the center of the error circle (J2000), in degrees; col. (5) is the BATSE declination of the center of the error circle (J2000), in degrees; col. (6) is the total 1 σ statistical BATSE error circle radius, in degrees (the approximate total 1 σ radius is obtained by adding 1°.6 in quadrature, but see Briggs et al. 1998a, 1998b for an improved error model); col. (7) is the right ascension of the center of the IPN (BATSE/*Ulysses*) annulus, epoch J2000, corrected to the heliocentric frame, in degrees; col. (8) is the declination of the center of the IPN (BATSE/*Ulysses*) annulus, epoch J2000, corrected to the heliocentric frame in degrees; col. (9) is the angular radius of the IPN (BATSE/*Ulysses*) annulus, corrected to the heliocentric frame, in degrees; and col. (10) is the half-width of the IPN (BATSE/*Ulysses*) annulus, in degrees. The 3 σ confidence annulus is given by $R_{\mathrm{IPN}} \pm \delta R_{\mathrm{IPN}}$.

this catalog. To generate this plot, it was assumed that all annuli pass through the centers of their corresponding BATSE error circles.

We stress that while the BATSE data are for the bursts listed in the 3B catalog, the locations and error circle radii are in fact the updated ones that will appear in the 4B catalog. They have been taken from the latest online catalog and are given here for convenience only.[3] Finally, we add that 150 *Ulysses*/BATSE bursts were detected over the period between the end of the 3B catalog and the end of the 4B catalog. Analysis of these events has been completed and is being published in conjunction with the 4B catalog.

[3] The catalog (http://www.batse.msfc.nasa.gov/data/grb/4bcatalog/) should be considered as the ultimate source of the most up-to-date BATSE data. Table 1 is available electronically from http://ssl.berkeley.edu/ipn3/index.html.

Support for the *Ulysses* GRB experiment is provided by JPL contract 958056. Joint analysis of *Ulysses* and BATSE data is supported by NASA grant NAG 5-1560. C. K. acknowledges support from NASA grant NAG5-2560.

REFERENCES

Briggs, M., et al. 1998a, ApJS, 118, 391
Briggs, M., Pendleton, G., Brainerd, J., Connaughton, V., Kippen, R. M., Meegan, C., & Hurley, K. 1998b, in AIP Conf. Proc. 428, Gamma-Ray Bursts: Fourth Huntsville Symp., ed. C. Meegan, R. Preece, & T. Koshut (New York: AIP), 104
Galama, T., et al. 1997, ApJ, 486, L5
Hurley, K. 1994, in AIP Conf. Proc. 307, Gamma-Ray Bursts, ed. J. Fishman, J. Brainerd, & K. Hurley (New York: AIP), 682
Hurley, K., et al. 1992, A&AS, 92(2), 401
———. 1996, BAAS, 28(4), 1408
———. 1997a, ApJ, 479, L113
———. 1997b, Proc. 25th Int. Cosmic Ray Conf., ed. M. Potgieter, B. Raubenheimer, & D. van der Walt (Singapore: World Scientific), 45
———. 1997c, ApJ, 485, L1
———. 1998a, in AIP Conf. Proc. 428, Gamma-Ray Bursts: Fourth Huntsville Symp., ed. C. Meegan, R. Preece, & T. Koshut (New York: AIP), 50
Hurley, K., et al. 1998b, Nucl. Phys. B, 69 (1–3), 660
Kippen, M., Hurley, K., & Pendleton, G. 1998, in AIP Conf. Proc. 428, Gamma-Ray Bursts: Fourth Huntsville Symp., ed. C. Meegan, R. Preece, & T. Koshut (New York: AIP), 114
Kolatt, T., & Piran, T. 1996, ApJ, 467, L41
Kulkarni, S., et al. 1998, Nature, 393, 35
Laros, J., et al. 1997, ApJS, 110, 157
———. 1998, ApJS, 118, 391
Meegan, C., et al. 1996, ApJS, 106, 45
Metzger, M., et al. 1997, Nature, 387, 878
Paczyński, B. 1991, Acta Astron., 41, 257
Schartel, N., Andernach, H., & Greiner, J. 1997, A&A, 323, 659
Struble, M., & Rood, H. 1997, ApJ, 490, 109
Tokanai, F., et al. 1997, PASJ, 49, 207